Mechanics Of Soft Materials
https://doi.org/10.1007/s42558-019-0004-2

ORIGINAL PAPER

The effect of local inertia around the crack-tip in dynamic fracture of soft materials

Anshul Faye[1] · **Yoav Lev**[2] · **K. Y. Volokh**[2]

Received: 3 January 2019 / Accepted: 25 January 2019

Abstract
Phase-field or gradient-damage approaches offer elegant ways to model cracks. Material stiffness decreases in the cracked region with the evolution of the phase-field or damage variable. This variable and, consequently, the decreased stiffness are spatially diffused, which essentially means the loss of the internal links and the bearing capacity of the material in a finite region. Considering the loss of material stiffness without the loss of inertial mass seems to be an incomplete idea when dynamic fracture is considered. Loss of the inertial mass in the damaged material region may have significant effect on the dynamic failure processes. In the present work, dynamic fracture is analyzed using a theory, which takes into account the local loss of both material stiffness and inertia. Numerical formulation for brittle fracture at large deformations is based on the Cosserat point method, which allows suppressing the hourglass type deformation modes in simulations. Based on the developed algorithms, the effect of the material inertia around a crack tip is studied. Two different problems with single and multiple cracks are considered. Results suggest that in dynamic fracture the localized loss of mass plays an important role at the crack tip. It is found, particularly, that the loss of inertia leads to lower stresses at the crack tip and, because of that, to narrower cracks as compared to the case in which no inertia loss is considered. It is also found that the regularized problem formulation provides global convergence in energy under the mesh refinement. At the same time, the local crack pattern might still depend on the geometry of the unstructured mesh.

Keywords Fracture · Material sink · Dynamic · Phase-field · Coupled · Inertia

1 Introduction

Understanding and modeling of the crack propagation is arguably the central problem in solid mechanics. Two major classes of approaches for analysis of crack propagation are surface and bulk material failure models, also known as Cohesive Surface Model (CSM) and Continuum Damage Model (CDM), respectively. CSM defines interaction between the separating surfaces using traction-separation laws [2, 7, 9, 11, 14, 25, 27, 35, 43, 50]. They are most effective when possible crack paths are already known. If the path is not known, then defining the criteria for nucleation and growth of cracks still remains a challenge [26]. On the other hand, CDM describes the failure via damage constitutive laws [5, 12, 15, 18, 20, 22, 23, 38, 44, 45, 49]. When using CDM, important features such as damage nucleation, propagation, and branching naturally derive from

✉ Anshul Faye
afaye@iitbhilai.ac.in

Yoav Lev
yoavlev@campus.technion.ac.il

K. Y. Volokh
cvolokh@technion.ac.il

[1] Department of Mechanical Engineering, Indian Institute of Technology Bhilai, Raipur, CG 492015, India

[2] Faculty of Civil and Environmental Engineering, Technion, Haifa, Israel

Published online: 01 February 2019

the constitutive laws. Unfortunately, numerical simulations based on the CDM are mesh sensitive: the finer meshes lead to the finer localized damage zones and lower dissipated energies [29–31]. Ultimately, damage can occur without the energy dissipation, which is physically meaningless.

To regularize CDMs by suppressing the pathological mesh sensitivity, nonlocal continuum formulations emerged [10, 21, 28, 33, 36]. These formulations naturally incorporate characteristic length as a parameter to limit the size of spatial damage localization The physical assumption underlying most nonlocal theories is long-range interaction of material particles. Unfortunately, actual interaction of particles is of short-range (on nanometers or angstrom length scale). Hence, the physical basis for nonlocal continuum models appears disputable.

A special class of gradient-type damage theories called phase-field approach is becoming increasingly popular for modeling fracture [6, 8, 13, 16, 19]. In this approach, the phase field variable (also known as the internal damage variable in the earlier literature) is introduced in order to decrease the material stiffness. Apparently, the macroscopic degradation of the material stiffness is triggered by the breakage of the atomic/molecular bonds. However, the material bond breakage should also be accompanied by the mass/inertia loss. Agrawal and Dayal [1] and Chen et al. [8] have raised such concerns when using phase-field method for modeling dynamic fracture. However, the simultaneous loss of stiffness and inertia is nothing but the *mass sink*. Volokh [48] sharpened the latter notion and formulated the regularized approach to fracture as a coupled hyperelastic-mass-diffusion problem.

In the present work, we first develop a numerical formulation for the theory given by [48]. Then, we use the finite element (FE) method to simulate fracture in a hyperelastic material. We consider two situations: (i) when the mass diffusion does not affect inertia and density only acts as a variable controlling the failure through stiffness. For this situation, the material in cracked regions has inertia even after failure but has no stiffness; (ii) when the material in cracked regions becomes massless due to diffusion of the mass to the surroundings. These two situations represent two extremes. Analysis of these situations gives us an insight on the effect of local inertia near the crack-tip on the crack growth. Numerical performance of the theory is also evaluated for different mesh size. Two different fracture problems with single and double cracks under dynamic loading are solved. The results show that the crack growth under dynamic conditions is significantly affected by the variation of inertia around the crack-tip.

The rest of the paper is organized as follows. In Section 2, we briefly present the theory and the constitutive model used for the numerical simulations. Details of the FE formulation for a plane strain Cosserat Point Element (CPE) and its implementation are presented in Section 3. Numerical results from simulations of the fracture problems are presented in Section 4. Finally, the salient conclusions from the study are presented in Section 5.

2 Theoretical formulation

The physical intuition underlying the theory can be briefly described as follows. Assume that crack is an ideal separation of two adjacent atomic/molecular layers. Then, the closed crack would have the thickness of the interatomic/intermolecular distance, which is on the scale of angstroms or, even, nanometers Fig. 1 (left). A naked eye, whose length resolution is on the scale of tens of microns, would be unable to identify cracks. However, we do see cracks! The latter means that the thickness of the closed crack is much greater than the thickness of one atomic layer. Thousands atomic layers are involved in the fracture process Fig. 1 (right). Bond breakage is diffused and, consequently, it is accompanied by the local loss of mass. The vision of the material separation as a result of the highly localized mass sink has been formalized in [48] and below we give a summary of the theory in the form, which will be further used in computational formulation and simulations.

2.1 Balance equations

In the context of continuum mechanics, consider a material point occupying a position $\boldsymbol{X}$ in the reference configuration Ω_0 of a deformable body, which moves to a position $\boldsymbol{x}$ in the current configuration Ω. Deformation in the vicinity of the material point is described by the deformation gradient,

$$\boldsymbol{F} = \frac{\partial \boldsymbol{x}}{\partial \boldsymbol{X}}. \tag{1}$$

The basic assumption of the theory is that failure and, consequently, mass flow are very localized and the momentum and energy balance equations can be written in standard form without adding momentum and energy due to the change in mass.

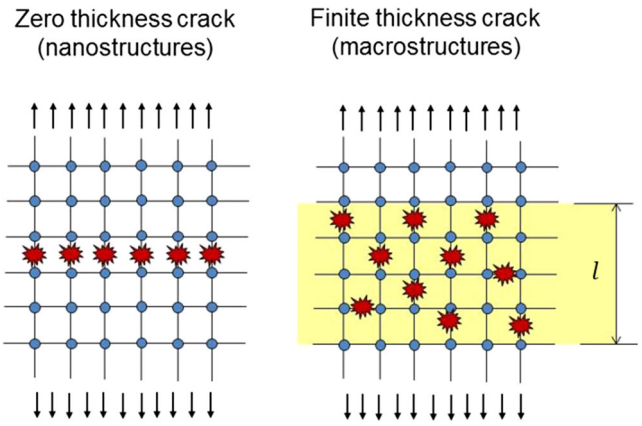

Fig. 1 Schematic drawing of cracks with zero or finite thickness.

Following the assumption, Eulerian form of momentum balance equation can be written as

$$\frac{d(\rho \boldsymbol{v})}{dt} = \text{div}\boldsymbol{\sigma} + \rho \boldsymbol{b}, \tag{2}$$

where ρ is the spatial mass density, $\boldsymbol{v}$ is the spatial velocity of a material point, $\boldsymbol{b}$ is the spatial body force per unit mass, and $\boldsymbol{\sigma}$ is the Cauchy stress tensor.

Further, Eulerian form of local mass balance equations is

$$\frac{d\rho}{dt} = \text{div}\boldsymbol{s} + \xi, \tag{3}$$

where $\boldsymbol{s}$ is the spatial mass flux and ξ is the spatial mass source (sink).

Further assumption is that the process of the bond breakage during fracture is very fast as compared to the dynamic deformation process and the mass density changes in time as a step function. The super fast transition to failure is not considered and it is assumed that the densities before and after failure are constants and hence,

$$\dot{\rho} = \text{div}\boldsymbol{s} + \xi = 0, \tag{4}$$

Considering (4), it can be shown that the second law of thermodynamics is satisfied.

Initial and boundary conditions are as follows. Natural boundary condition for zero mass flux representing the mass balance at the boundary $\partial\Omega$ as

$$\boldsymbol{s} \cdot \boldsymbol{n} = 0, \tag{5}$$

where $\boldsymbol{n}$ is the unit outward normal to the boundary in the current configuration. Natural boundary condition for applied traction $\bar{\boldsymbol{T}}$, representing the liner momentum balance on the boundary $\partial\Omega$ as

$$\boldsymbol{\sigma n} = \bar{\boldsymbol{T}}, \tag{6}$$

or, alternatively, the essential boundary conditions for placements $\boldsymbol{x}$ on $\partial\Omega$ as

$$\boldsymbol{x} = \bar{\boldsymbol{x}}. \tag{7}$$

Initial conditions in Ω are

$$\boldsymbol{x}(t=0) = \boldsymbol{x}_0, \boldsymbol{v}(t=0) = \boldsymbol{v}_0. \tag{8}$$

2.2 Constitutive equations

Constitutive law for the mass source follows from [48], which is given as

$$\xi(\rho, \rho_0, w, \phi) = \beta \left(\rho_0 H(\zeta)\ \exp[-(w/\phi)^m] - \rho\right), \tag{9}$$

where $\rho_0 = \rho(t=0)$ is the constant initial density; $\beta > 0$ is a material constant; w is the specific Helmholtz free energy function per unit mass; ϕ is the specific energy limiter per unit mass; m controls the sharpness of the transition to material failure on the stress-strain curve; and $H(\zeta)$ is a unit step function, i.e., $H(\zeta) = 0$ if $\zeta < 0$ and $H(\zeta) = 1$ otherwise. The

switch parameter ζ is necessary to prevent the material healing. The evolution equation for switch parameter $\zeta \in (-\infty, 0]$ is given as

$$\dot{\zeta} = -H\left(\epsilon - \frac{\rho}{\rho_0}\right), \quad \zeta(t=0) = 0, \tag{10}$$

where $0 < \epsilon \ll 1$ is a dimensionless precision constant. It should be noted that the evolution equation (10) is different from the one used in [48]. Equation (10) is more natural and stringent in the context of the numerical formulation.

Constitutive law for the Eulerian mass flux is written by analogy with the Fourier law for heat conduction as

$$\boldsymbol{s} = kH(\zeta)\exp[-(w/\phi)^m]\ \text{grad}\ \rho, \tag{11}$$

where $k > 0$ is the mass conductivity for isotropic case. The exponential term in (11) is required to suppress diffusion in the failed material. Substituting (11) and (9) to (4) yields,

$$\text{div}\left(l^2 H(\zeta)\exp\left[-\left(\frac{w}{\phi}\right)^m\right]\text{grad}\ \frac{\rho}{\rho_0}\right) + H(\zeta)\exp\left[-\left(\frac{w}{\phi}\right)^m\right] - \frac{\rho}{\rho_0} = 0, \tag{12}$$

where

$$l = \sqrt{\frac{k}{\beta}}, \tag{13}$$

is the characteristic length, which might depend on the deformation process. *It is important to mention that we do not need k and β separately, only the knowledge of the characteristic length is enough.*

For homogeneous deformation and mass flow, the first term on the left-hand side of (12) vanishes and we obtain

$$\rho = \rho_0 H(\zeta)\exp\left[-\left(\frac{w}{\phi}\right)^m\right]. \tag{14}$$

Substituting (14) in the hyperelastic constitutive law,

$$\boldsymbol{\sigma} = \frac{2}{J}\rho\boldsymbol{F}\frac{\partial w}{\partial \boldsymbol{C}}\boldsymbol{F}^T, \tag{15}$$

yields,

$$\begin{aligned}\boldsymbol{\sigma} &= \frac{2}{J}\rho_0 H(\zeta)\exp\left[-\left(\frac{w}{\phi}\right)^m\right]\boldsymbol{F}\frac{\partial w}{\partial \boldsymbol{C}}\boldsymbol{F}^T \\ &= \frac{2}{J}H(\zeta)\exp\left[-\left(\frac{W}{\Phi}\right)^m\right]\boldsymbol{F}\frac{\partial W}{\partial \boldsymbol{C}}\boldsymbol{F}^T,\end{aligned} \tag{16}$$

where

$$W = \rho_0 w, \quad \Phi = \rho_0 \phi, \tag{17}$$

are the Helmholtz free energy and energy limiter per unit referential volume, accordingly. $\boldsymbol{C}$ is the right Cauchy-Green tensor.

Constitutive law (16) is very similar to the hyperelasticity with the energy limiters, except with a different evolution equation for ζ. For the sake of brevity, details regarding the theory of energy limiters are not presented here. Readers are referred to [45–47] for details.

In the present work, for the application of the theory, we use a hyperelastic constitutive model representing the response of Abdominal Aortic Aneurysm (AAA)–A localized enlargement of the abdominal blood vessel named "aorta." Energy function W is given as

$$W(\boldsymbol{C}) = c_1(I_1 - 3) + c_2(I_1 - 3)^2, \quad \text{with} \quad I_3 = 1, \tag{18}$$

where c_1 and c_2 are material parameters, and I_1 and I_3 are the first and third invariant of $\boldsymbol{C}$.

Uniaxial response for (18) can be obtained by using (16). Fitting the uniaxial response from (16) to the experimental data by [34], parameters c_1, c_2 and Φ for AAA material can be obtained. To obtain these parameters, m is considered to be 10. The parameters are listed in Table 1. Theoretical stress-stretch curve for AAA material is compared to the experimental response in Fig. 2. Satisfactory agreement between them is obtained.

Table 1 Parameters for AAA material

c_1 (MPa)	c_2 (MPa)	Φ (MPa)	m
0.617	1.215	0.1686	10

2.2.1 Nearly incompressible form

In the context of FE simulations, a modified form of hyperelastic energy function (18) is used to model near incompressibility, which is as follows

$$\bar{W}(\boldsymbol{C}) = \rho_0 \bar{w}(\boldsymbol{C}) = c_1(\bar{I}_1 - 3) + c_2(\bar{I}_1 - 3)^2 + U(J), \tag{19}$$

where $\bar{I}_1$ is the first invariant of distortional component of $\boldsymbol{C}$, i.e., $J^{-2/3}\boldsymbol{C}$, and $U(J)$ is the volumetric energy function given as

$$U(J) = \frac{1}{2}\kappa(J-1)^2, \tag{20}$$

where κ is a large penalty modulus. $\kappa = 500$ MPa is used for all numerical simulations. Equation 19 will be used in later sections.

3 Numerical formulation and implementation

In this section, numerical formulation and implementation of the theory discussed in Section 2 is presented. Numerical solution of (2) and (12) requires spatial and temporal discretization. It is well known that the conventional finite element approach exhibits locking behavior when used for nearly incompressible materials. To overcome this deficiency, various element technologies such as hybrid formulation [32], reduced integration with hourglass control [3, 4], and enhanced assumed strains [37, 39] are developed. Although each of the abovementioned approach helps overcoming some of the known deficiency, they may have drawbacks [24]. The Cosserat Point Element (CPE) has been proven to be robust when considering typical locking phenomena (for poor element aspect ratios and nearly incompressible material response) compared to other standard finite elements [17]. Hence, in the present work, we follow Cosserat point approach for spatial discretization of momentum equation (2), which is briefly discussed in this section. For spatial discretization (12), the standard Galerkin method is used. Implementation of the element formulation, the time integration scheme, the element deletion criteria, and calculation of dissipated energy are also discussed.

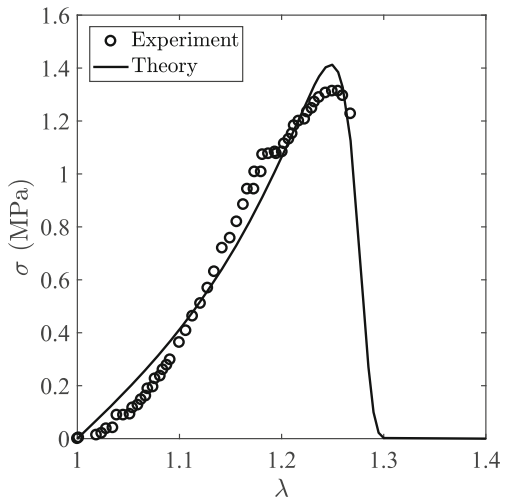

Fig. 2 Stress-stretch curve for AAA material

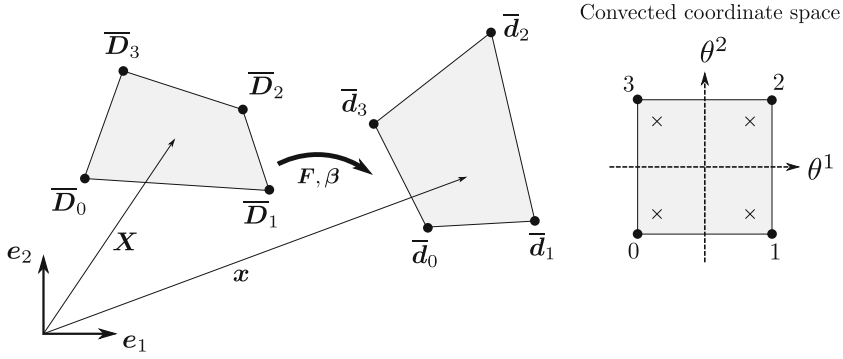

Fig. 3 A general quadrilateral CPE showing the reference configuration, the current configuration, the convected coordinate space and the nodal numbering. × showing the Gauss points for numerical integration at standard locations

3.1 Basic equations for a plane strain quadrilateral CPE

We briefly present the formulation for a plane strain CPE by [24]. A slightly different notation from [24] is used. Unless explicitly mentioned, in the following description, capital letters in subscript and/or superscript are used for nodal values and they take values as (0, 1, 2, 3). Small letters in subscript and/or superscript are used for dimensional components, which take values as (1, 2) for two-dimensional cases.

3.1.1 Kinematics

The reference and current configuration of plane strain quadrilateral CPE is shown in Fig. 3. Nodal locations of the element are given by nodal directors $\bar{\boldsymbol{D}}_I$ and $\bar{\boldsymbol{d}}_I$ in the reference and current configuration, respectively. The position vector $\boldsymbol{X}$ of a material point in the reference configuration moves to position $\boldsymbol{x}$ in the current configuration at time t. Position vectors are

$$\boldsymbol{X} = \sum_{J=0}^{3} N^J\left(\theta^i\right)\boldsymbol{D}_J, \quad \boldsymbol{x} = \sum_{J=0}^{3} N^J\left(\theta^i\right)\boldsymbol{d}_J, \tag{21}$$

where $\{\boldsymbol{D}_I, \boldsymbol{d}_I\}$ are the reference and current element director vectors, respectively; θ_i are convected coordinates $(-1/2 \leq \theta^i \leq 1/2)$ and N^I are the bilinear shape functions for node I, defined as

$$N^0 = 1,\ N^1 = \theta^1,\ N^2 = \theta^2,\ N^3 = \theta^1\theta^2. \tag{22}$$

Furthermore, the element directors $\{\boldsymbol{D}_1, \boldsymbol{D}_2\}$ and $\{\boldsymbol{d}_1, \boldsymbol{d}_2\}$ are restricted to be linearly independent, i.e.,

$$D^{1/2} = \boldsymbol{D}_1 \times \boldsymbol{D}_2 \cdot \boldsymbol{e}_3 > 0, \quad d^{1/2} = \boldsymbol{d}_1 \times \boldsymbol{d}_2 \cdot \boldsymbol{e}_3 > 0. \tag{23}$$

where $\boldsymbol{e}_3$ denotes the unit vector in 3–direction.

The element directors are related to the nodal directors as

$$\boldsymbol{D}_I = \sum_{J=0}^{3} A_{IJ}\bar{\boldsymbol{D}}_J, \quad \boldsymbol{d}_I = \sum_{J=0}^{3} A_{IJ}\bar{\boldsymbol{d}}_J. \tag{24}$$

where A_{IJ} is a constant matrix given as

$$[A_{IJ}] = \frac{1}{4}\begin{bmatrix} +1 & +1 & +1 & +1 \\ -2 & +2 & +2 & -2 \\ -2 & -2 & +2 & +2 \\ +4 & -4 & +4 & -4 \end{bmatrix}. \tag{25}$$

It should be emphasized that element shape functions (22) are related to the standard isoparametric shape functions $(\bar{N}^I)$ as

$$\bar{N}^I = \sum_{J=0}^{3} A_{JI}N^J. \tag{26}$$

Further, density at any point of the element is given as

$$\rho = \sum_{I=0}^{3} \bar{N}^I(\theta^i)\rho^I, \tag{27}$$

where ρ^I is the density at the I^{th} node of the element.

Deformation of the quadrilateral CPE is defined by a tensor $\boldsymbol{F}$ associated with homogeneous deformation, and a vector $\boldsymbol{\beta}$ associated with inhomogeneous deformation, so that

$$\boldsymbol{F} = \sum_{i=1}^{2} \boldsymbol{d}_i \otimes \boldsymbol{D}^i, \quad \boldsymbol{\beta} = \boldsymbol{F}^{-1}\boldsymbol{d}_3 - \boldsymbol{D}_3, \tag{28}$$

where $\boldsymbol{D}^i$ are the reciprocal vectors of $\boldsymbol{D}_i$.

The CPE uses a volume average deformation gradient ($\bar{\boldsymbol{F}}$), which is similar to under integration for standard finite elements. For plane strain quadrilateral CPE it can be shown that,

$$\bar{\boldsymbol{F}} = \boldsymbol{F} = \sum_{i=1}^{2} \boldsymbol{d}_i \otimes \boldsymbol{D}^i. \tag{29}$$

Finally, inhomogeneous strains b_i for the two bending modes of two dimensional elements are given as

$$b_1 = \boldsymbol{\beta} \cdot \boldsymbol{D}^1, \quad b_2 = \boldsymbol{\beta} \cdot \boldsymbol{D}^2. \tag{30}$$

3.1.2 Constitutive equations

In CPE formulation, an element is considered as a structure with a strain energy function characterizing its response. This strain energy function (per unit mass) ψ can be additively decomposed into two parts, one part ψ_{H} corresponding to the homogeneous and another part ψ_{I} corresponding to the inhomogeneous deformations, so that

$$\psi = \psi_{\text{H}}\left(\bar{\boldsymbol{C}}\right) + \psi_{\text{I}}\left(\Upsilon\right), \tag{31}$$

where,

$$\bar{\boldsymbol{C}} = \bar{\boldsymbol{F}}^T\bar{\boldsymbol{F}} + \boldsymbol{e}_3 \otimes \boldsymbol{e}_3, \tag{32}$$

is the volume average of $\boldsymbol{C}$. Here, $\psi_{\text{H}}\left(\bar{\boldsymbol{C}}\right)$ is nothing but the strain energy function $\bar{w}(\bar{\boldsymbol{C}})$, given by (19). The set Υ in (31) includes dependence on element dimensions (H_1, H_2), the metric D_{12} and material constants. These quantities are defined as

$$H_1 = \|\boldsymbol{D}_1\|, \quad H_2 = \|\boldsymbol{D}_2\|, \quad D_{12} = \frac{\boldsymbol{D}_1 \cdot \boldsymbol{D}_2}{H_1 H_2}. \tag{33}$$

Further, in order to ensure that the CPE satisfies a nonlinear form of the patch test, strain energy function controlling the inhomogeneous deformations has to be restricted. It can be shown that the CPE automatically satisfies the patch test when ψ_{I} has the following form,

$$\psi_{\text{I}} = \frac{V}{2\bar{\rho}v} B_{ij} b_i b_j, \quad B_{ij} = B_{ji} = B_{ij}(\Upsilon). \tag{34}$$

where V and v are the reference and current volume per unit depth, respectively, and $\bar{\rho} = \rho(\theta_1 = 0, \theta_2 = 0)$ is the density at the center point of the element, which can be calculated using (27).

Now, within the context of pure mechanical theory, the rate of dissipation of hyperelastic material vanishes and can be written in the following form,

$$d^{1/2}D = d^{1/2}\boldsymbol{\sigma} : \boldsymbol{D} + \boldsymbol{F}^T\boldsymbol{t}^3 \cdot \dot{\boldsymbol{\beta}} - \bar{\rho}v\dot{\psi} = 0, \tag{35}$$

where $\boldsymbol{D}$ is the rate of deformation tensor, $\boldsymbol{t}^I$ are the intrinsic director couples, and $\boldsymbol{\sigma}$ is the Cauchy stress tensor. Using (31) and (35) and assuming that $d^{1/2}\boldsymbol{\sigma}$ and $\boldsymbol{t}^I$ are independent of the rates $\boldsymbol{D}$, $\dot{\beta}$, it follows that

$$d^{1/2}\boldsymbol{\sigma} = \frac{2}{\bar{J}} V \bar{\rho} \bar{\boldsymbol{F}} \frac{\partial \psi_{\mathrm{H}}}{\partial \bar{\boldsymbol{C}}_{2\mathrm{D}}} \bar{\boldsymbol{F}}^T, \text{ where } \bar{\boldsymbol{C}}_{2\mathrm{D}} = \bar{\boldsymbol{F}}^T \bar{\boldsymbol{F}}, \tag{36}$$

$$\boldsymbol{t}^3 = V(B_{11}b_1 + B_{12}b_2)\boldsymbol{d}^1 + V(B_{21}b_1 + B_{22}b_2)\boldsymbol{d}^2, \tag{37}$$

$$\boldsymbol{t}^i = \left(d^{1/2}\boldsymbol{\sigma} - \boldsymbol{t}^3 \otimes \boldsymbol{d}_3\right)\boldsymbol{d}^i \quad (i = 1, 2), \tag{38}$$

where $\bar{J} = \det(\bar{F})$. The constitutive coefficients B_{ij} in (34) are determined by matching the solutions of the linearized equations for the CPE with exact solutions of the linear theory of elasticity for a special shaped element. Here, we only give the formulae for B_{ij} for an isotropic material. Readers interested in derivation of these formulae are refereed to [24].

$$B_{11} = \frac{K}{12}\left[1 + \left(\frac{D_{12}H_1}{H_2}\right)^2\right], \tag{39}$$

$$B_{12} = B_{21} = \frac{K}{12} D_{12}\left(\frac{H_2}{H_1} + \frac{H_1}{H_2}\right), \tag{40}$$

$$B_{22} = \frac{K}{12}\left[1 + \left(\frac{D_{12}H_2}{H_1}\right)^2\right], \tag{41}$$

$$K = \frac{4\mu\,(\lambda + \mu)}{\lambda + 2\mu}. \tag{42}$$

where λ and μ are initial Lames' constant in the undeformed state of the material.

3.1.3 Weak form of the momentum equation

Following the standard Bubnov-Galerkin procedure, the weak form of the momentum Eq. 2 is obtained by multiplying the nodal shape functions $\bar{N}_I$ and then integrating over the element region Ω_e, which results in

$$\bar{\boldsymbol{M}}^{IJ}\ddot{\boldsymbol{d}}_J = \boldsymbol{f}^I_{\mathrm{ext}} - \boldsymbol{f}^I_{\mathrm{int}}, \tag{43}$$

where $\bar{\boldsymbol{M}}^{IJ}$ is the mass matrix; $\boldsymbol{f}^I_{\mathrm{ext}}$ is the external nodal force vector due to body forces and surface tractions. These quantities are given as

$$\bar{\boldsymbol{M}}^{IJ} = \boldsymbol{I}\int_{\Omega_e} \bar{\rho}\,\bar{N}^I\bar{N}^J dv, \tag{44}$$

$$\boldsymbol{f}^I_{\mathrm{ext}} = \int_{\Omega_e} \bar{N}^I \bar{\rho}\boldsymbol{b} dv + \int_{\partial\Omega_e} \bar{N}^I \boldsymbol{T} ds = \sum_{J=0}^{7} A_{JI}\left[\int_{\Omega_e} \bar{N}^J \bar{\rho}\boldsymbol{b} dv + \int_{\partial\Omega_e} \bar{N}^J \boldsymbol{T} ds\right],$$

where $\boldsymbol{I}$ is a unit matrix; dv and ds are the volume and area of element per unit depth in the present configuration, respectively, and $\boldsymbol{T}$ is the surface traction vector. The quantity $\boldsymbol{f}^I_{\mathrm{int}}$ is the nodal internal forces and is related to intrinsic director couples $\boldsymbol{t}^I$, as follows

$$\boldsymbol{f}^I_{\mathrm{int}} = A_{JI}\boldsymbol{t}^J \quad \text{with} \quad \boldsymbol{t}^0 = \boldsymbol{0}. \tag{45}$$

Finally, the element residual vector for the momentum equation is

$$\boldsymbol{R}^u = \boldsymbol{f}^I_{\mathrm{ext}} - \boldsymbol{f}^I_{\mathrm{int}} - \bar{\boldsymbol{M}}^{IJ}\ddot{\boldsymbol{d}}_J. \tag{46}$$

3.2 Weak form of the mass balance equation

Following the standard Bubnov-Galerkin approach, the weak form of the mass balance Eq. 12 for an element can be written as

$$\int_{\Omega_e} H(\zeta)\exp\left[-\left(\frac{W}{\Phi}\right)^m\right]\frac{l^2}{\rho_0}\frac{\partial\rho}{\partial x_i}\frac{\partial\bar{N}^I}{\partial x_j}\,dv - \int_{\Omega_e}\left(H(\zeta)\exp\left[-\left(\frac{W}{\Phi}\right)^m\right] - \frac{\rho}{\rho_0}\right)\bar{N}^I\,dv = 0. \tag{47}$$

Strain energy for the element will be calculated using the average deformation gradient (29), which yields a constant $\bar{W}$ for the element. Thus, (47) can be rewritten as

$$\int_{\Omega_e} \left(\frac{l^2}{\rho_0} \frac{\partial \bar{N}^I}{\partial x_i} \frac{\partial \bar{N}^J}{\partial x_j} + \frac{\bar{N}^I \bar{N}^J}{\rho_0 H(\zeta) \exp\left[-\left(\frac{W}{\Phi}\right)^m \right]} \right) \rho^I \, dv - \int_{\Omega_e} \bar{N}^I dv = 0. \tag{48}$$

Approximation (27) is used while writing (48). Now, element level equations for mass balance are given as

$$\boldsymbol{K}^\rho \boldsymbol{\rho} = \boldsymbol{F}^\rho. \tag{49}$$

where $\boldsymbol{\rho}$ is the vector of nodal densities. $\boldsymbol{K}^\rho$ and $\boldsymbol{F}^\rho$ are the element stiffness and the element force vector for the mass balance equation, which are given as

$$\boldsymbol{K}^\rho = \int_{\Omega_e} \left[\frac{l^2}{\rho_0} \frac{\partial \bar{\boldsymbol{N}}}{\partial \boldsymbol{x}}^T \frac{\partial \bar{\boldsymbol{N}}}{\partial \boldsymbol{x}} + \frac{\bar{\boldsymbol{N}}^T \bar{\boldsymbol{N}}}{\rho_0 H(\zeta) \exp\left[-\left(\frac{W}{\Phi}\right)^m \right]} \right] dv, \tag{50}$$

$$\boldsymbol{F}^\rho = \int_{\Omega_e} \bar{\boldsymbol{N}} dv. \tag{51}$$

The element residual vector for the mass balance equation is

$$\boldsymbol{R}^\rho = \boldsymbol{F}^\rho - \boldsymbol{K}^\rho \boldsymbol{\rho}. \tag{52}$$

3.3 Numerical implementation and time integration scheme

The FE formulation presented in Sections 3.1 and 3.2 is implemented as a user element in finite element program FEAP v8.4 [40, 41]. For solution of the FE equations, we follow a staggered time discretization scheme in which momentum and mass balance equations are solved independently at a given time step. This is facilitated by the "PARTITION" command in FEAP [42]. Apart from reducing the problem to two smaller systems, this scheme allows us to choose different integration schemes for momentum and mass balance equations. First, displacements are obtained by solving momentum equations using the explicit Newmark-β method with numerical damping ($\beta = 0, \gamma = 0.6$) [42]. This method requires diagonal mass matrix, which is obtained by the row sum technique. As the explicit Newmark-β method is conditionally stable, sufficiently small time steps are ensured by implementing automatic time stepping through a user macro [41]. Next, solution of the mass balance equation is obtained by direct inversion of the stiffness matrix, at the same time step. The shape of the element stiffness matrix and the element residual in user subroutine for the coupled element will be as follows,

$$\mathbb{K}^e = \begin{bmatrix} \boldsymbol{K}^u_{IJ} & \boldsymbol{0} \\ \boldsymbol{0} & K^\rho_I \end{bmatrix}, \quad \mathbb{R}^e = \begin{bmatrix} \boldsymbol{R}^u_I \\ R^\rho_I \end{bmatrix} \tag{53}$$

In the present solution scheme, $\boldsymbol{K}^u = 0$ is used, because the explicit method for solution of the momentum equation requires only the element residual (46) to be defined in the user element subroutine.

3.4 Element deletion criterion and calculation of energy dissipation

For numerical implementation step function $H(\zeta)$ is simply replaced by a flag variable $\mathcal{H}$ in (50). Thus (50) now reads,

$$\boldsymbol{K}^\rho = \int_{\Omega_e} \left[\frac{l^2}{\rho_0} \frac{\partial \bar{\boldsymbol{N}}}{\partial \boldsymbol{x}}^T \frac{\partial \bar{\boldsymbol{N}}}{\partial \boldsymbol{x}} + \frac{\bar{\boldsymbol{N}}^T \bar{\boldsymbol{N}}}{\rho_0 \mathcal{H} \exp\left[-\left(\frac{W}{\Phi}\right)^m \right] + \varepsilon} \right] dv, \tag{54}$$

where $0 < \varepsilon \ll 1$ is a dimensionless precision constant, which avoids numerical instabilities due to $\boldsymbol{K}$ becoming ∞ when $\mathcal{H} = 0$ (for deleted elements). $\varepsilon = 1 \times 10^{-10}$ is used for all numerical simulations.

Initially, $\mathcal{H} = 1$ for all elements. At each time step, densities at the Gauss points (shown in Fig. 3) of an element are compared with the critical density $\rho_{cr} = \epsilon\rho$, where ϵ defines the criteria for deletion. At some time $t = t_d$, when the condition $\rho \leq \rho_{cr}$ is satisfied at all the Gauss points of the element, the value of $\mathcal{H}$ for the element becomes 0 and it remains equal to 0 for all $t > t_d$ during the simulation. Such elements with $\mathcal{H} = 0$ will be called deleted elements.

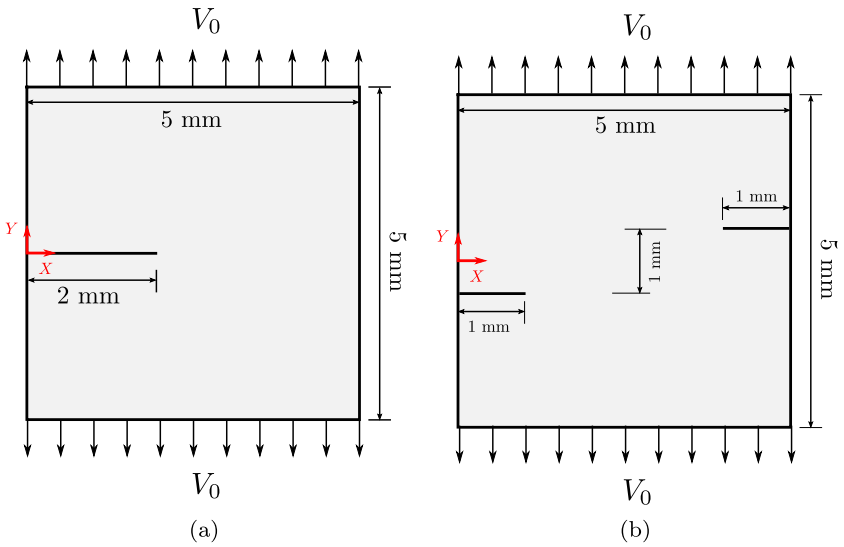

Fig. 4 Schematic presentation of the crack problems. **a** Mode-I crack problem and **b** double crack problem, under dynamic loading

Deleted elements are not removed from the mesh. Random distortions in such elements cause non-physical values for quantities, which involve current coordinates (e.g., deformation gradient $\boldsymbol{F}$). This results in unnecessary termination of the simulation. To avoid such difficulties the following approximations are required:

- For deleted elements, the internal force vector $\boldsymbol{f}^I_{\text{int}} = \boldsymbol{0}$ in (46) and all calculations for $\boldsymbol{f}^I_{\text{int}}$ are skipped.
- Ideally for any node the minimum value of ρ is 0. Hence for the deleted element $\bar{\rho} \to 0$. Zero elements in the global mass matrix are not desired. Hence, for a deleted element $\bar{\rho} = \rho_{cr}/4$ is used for the calculation of lumped mass matrix .
- For the deleted elements first term is removed from (50), as it involves gradient calculation w.r.t current coordinates.

The energy dissipation (U_d) due to formation of cracks is simply calculated as

$$U_d = \Phi \sum_{i=1}^{E_N} A_e^i, \tag{55}$$

where E_N is the number of deleted elements (i.e., $\mathcal{H} = 0$) and A_e is the reference area per unit depth of the i^{th} element. It should be emphasized that the dissipation energy due to partial decrease in density around the crack is not considered, in order to keep the calculations simple.

4 Numerical results

We investigate the performance of the method for modeling of fracture with different mesh size. Two different problems are considered; Mode-I crack and a system of two cracks as shown in Fig. 4a and b, respectively, are analyzed under dynamic loading.

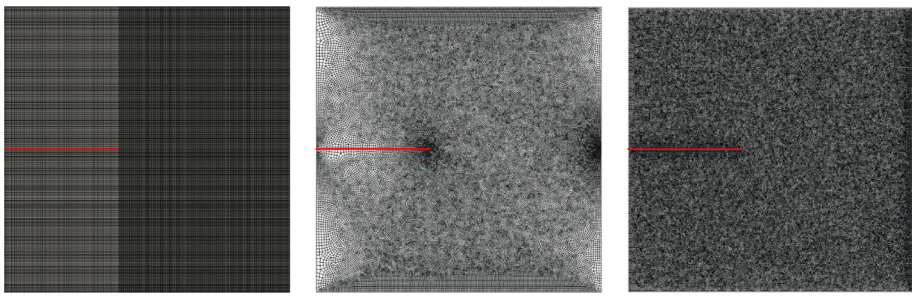

(a) S_1 (b) S_2 (c) S_3

Fig. 5 Different meshes for Mode-I crack problem. Thick red lines indicate the initial crack

Table 2 Details of the meshes S_1 to S_3

	No. of element	Min. edge length (mm)	Avg. min. edge length (mm)
S_1	105000	0.0120	0.0133
S_2	54854	0.0058	0.0188
S_3	119247	0.00275	0.0128

In dynamic fracture the role of inertia around the crack-tip is significant. To study the effect of local inertia near the crack-tip on crack propagation, two possibilities are considered, which are as follows.

- Case I – Element mass is always calculated using a constant value (ρ_0) of density. Thus, elements never loose mass, even after deletion. Density is treated as a variable affecting only the stiffness and not the inertia.
- Case II – Element mass is calculated using current values (ρ) of density. When the cracks are formed by diffusion of density to the surroundings, the crack-tip is surrounded by a region having very low mass and deleted elements are almost massless.

For all simulations the characteristic length $l = 0.1$ mm is used.

4.1 Mode-I crack problem

Geometry and loading for the problem are shown in Fig. 4a. Three different meshes, S_1 to S_3, are considered for the analysis, which are shown in Fig. 5. S_1 is structured mesh whereas S_2 and S_3 are unstructured meshes. Details of the meshes are given in Table 2. In all the meshes, the minimum element size is very small compared to the characteristic length l. Though the problem is symmetric, a full problem is modeled to analyze the effect of unstructured (and asymmetric) mesh on the crack propagation. A constant velocity $V_0 = 4$ m/s is applied at the ends $y = \pm 2.5$ mm.

4.1.1 Case I

For this case, inertia of the elements remains constant during the simulation. $\epsilon = 0.001\rho_0$ is used for element deletion. Contours of the normalized density (ρ/ρ_0) (which also indicate cracks) are shown in Fig. 6 for S_1 to S_3 at $t = 185$ μs, in the reference configuration. For visualization purpose, the initial crack is shown by a thick black line. Corresponding meshes with deleted elements (shown in blue colors) are also shown in the same figure. It is observed that the fracture patterns are not exactly the same, however branching of the crack is captured by all meshes (S_1 to S_3). As expected, for structured mesh S_1 crack patterns are symmetric whereas, for unstructured meshes S_2 and S_3 the degree of asymmetry in the crack pattern

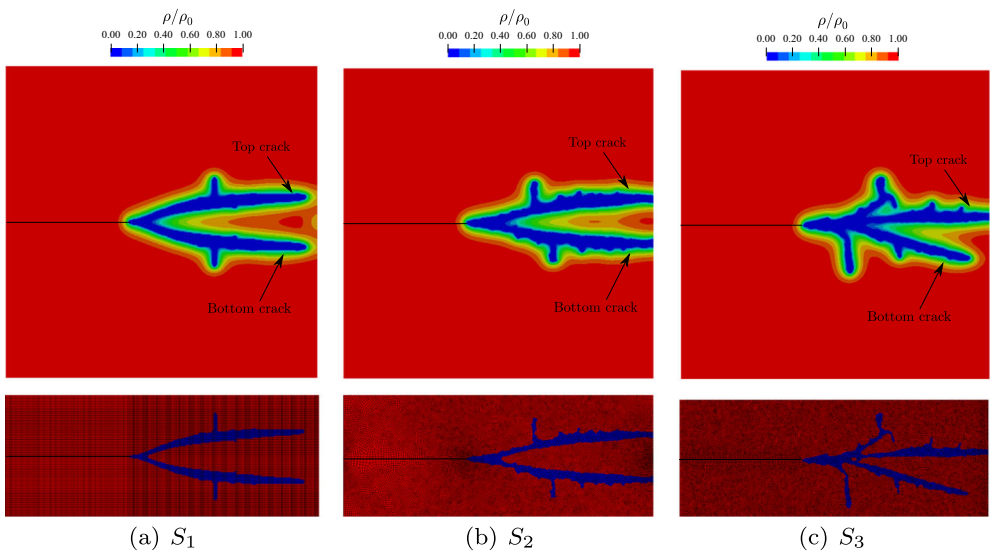

Fig. 6 Mode-I crack problem—case 1: contours of ρ/ρ_0 for S_1 to S_3 at $t = 185$ μs. Deleted elements are also shown for corresponding mesh at the bottom of each figure. The initial crack is shown by a thick black line

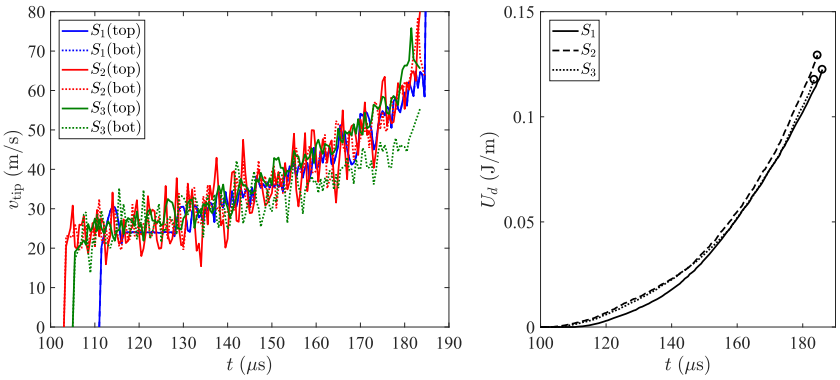

Fig. 7 Mode-I crack problem—case 2: crack-tip velocity and dissipation energy

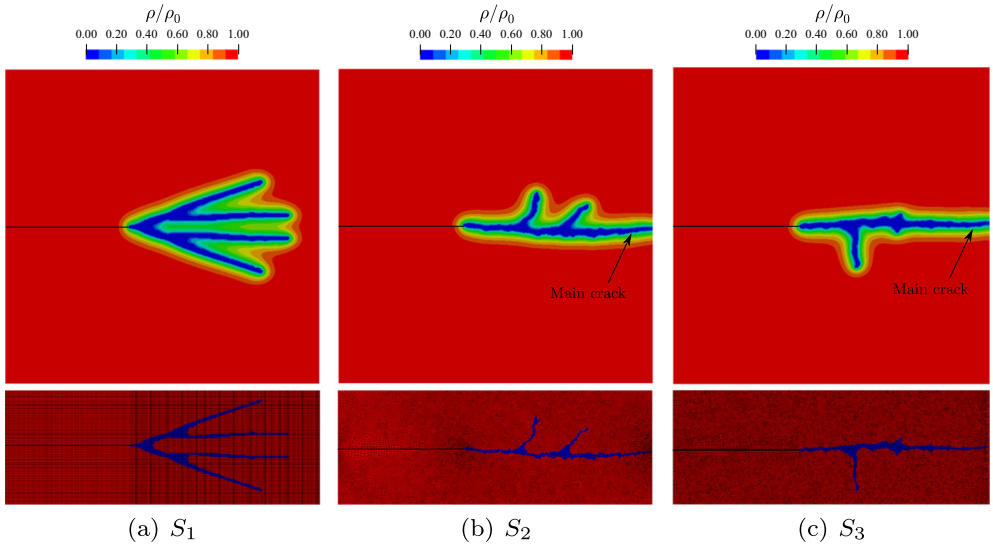

Fig. 8 Mode-I crack problem—case II: contours of ρ/ρ_0 for S_1 to S_3 at $t = 167$ μs. Deleted elements are also shown for corresponding mesh at the bottom of each figure. The initial crack is shown by a thick black line

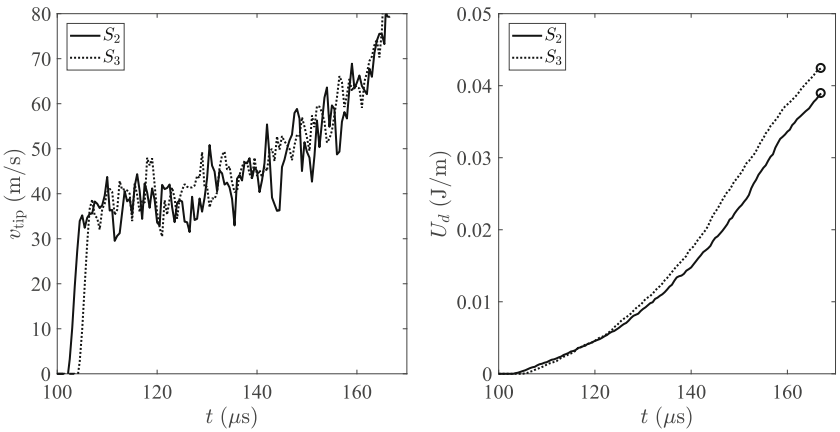

Fig. 9 Mode-I crack problem—case II: crack-tip velocity and dissipation energy

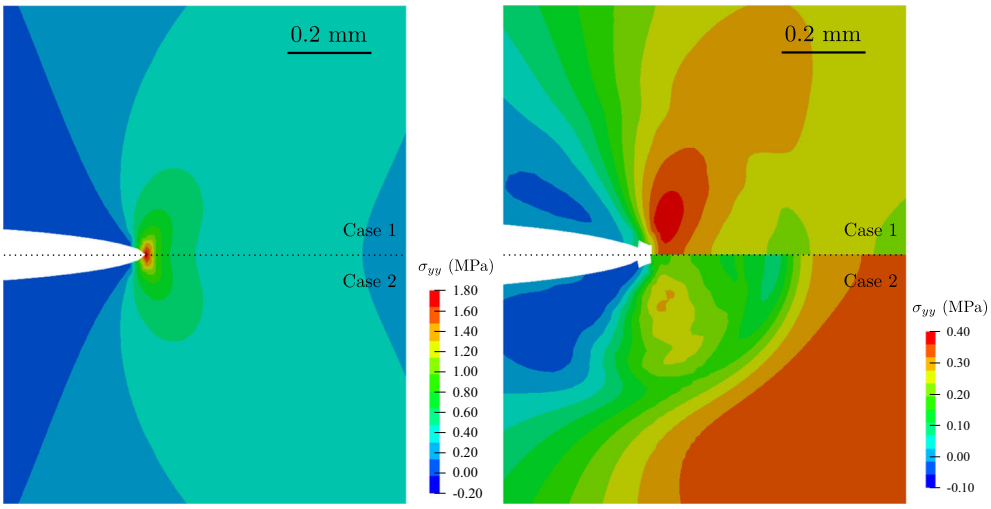

(a) Before failure ($t = 106\mu$s) (b) After failure ($t = 112\mu$s)

Fig. 10 Opening stress σ_{yy} near the crack-tip at time **a** $t = 106$ μs, **b** $t = 112$ μs. Upper and lower halves show the stresses from cases I and II, respectively

depends upon the mesh. The most asymmetric crack pattern is observed for S_3 (Fig. 6c). For S_1 the crack has not reached to boundary, unlike S_2 and S_3, due to relatively coarse mesh [6]. It is also observed that more sub-cracks appear from the main cracks, as element size becomes smaller.

Crack-tip velocity (v_{tip}) of top and bottom cracks for S_1 to S_3 are plotted in Fig. 7a, which is mainly governed by the applied velocity V_0. For all meshes, crack-tip velocity remains almost the same, except for the bottom crack in S_3. Crack initiation time decreases and seems to converge with the mesh becoming finer. Energy dissipation U_d for all meshes are plotted in Fig. 7b, till the time in which at least one of the crack reaches boundary (final point is indicated by an open circle). Energy dissipation history and the final values of U_d for all meshes are not very different from each other.

For meshes coarser than S_1 to S_3, stress fields of the top and bottom cracks start interacting before they reach the boundary, which causes stress to increase at a point somewhere between these cracks. This results in different crack patterns from those in Fig. 6. For the sake of completeness, we present results for the coarser meshes (both structured and unstructured) in A. Details of these meshes are given in Table 4 in Appendix 1. Contours of ρ/ρ_0 at the instant when the interaction of cracks starts fracture and the final crack pattern at time $t = 189$ μs are shown in Fig. 15 in Appendix 1.

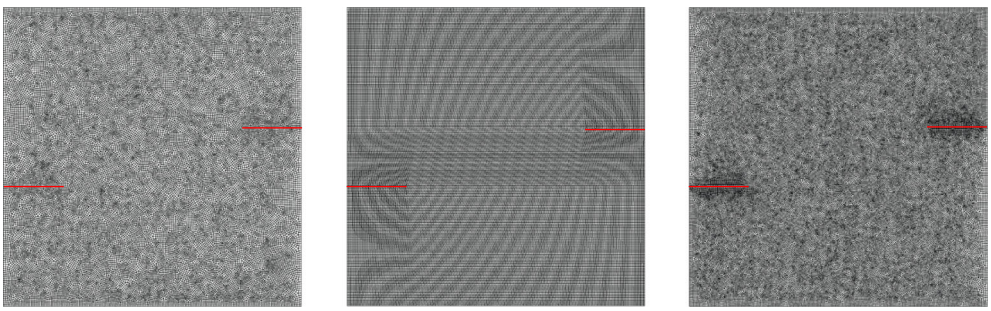

(a) D_1 (b) D_2 (c) D_3

Fig. 11 Different meshes for the double crack problem. Thick red lines indicate the initial crack

Table 3 Details of the meshes D_1 to D_3

	No. of element	Min. edge length (mm)	Avg. min. edge length (mm)
D_1	33960	0.0103	0.0240
D_2	46800	0.0167	0.0192
D_3	54418	0.00281	0.0190

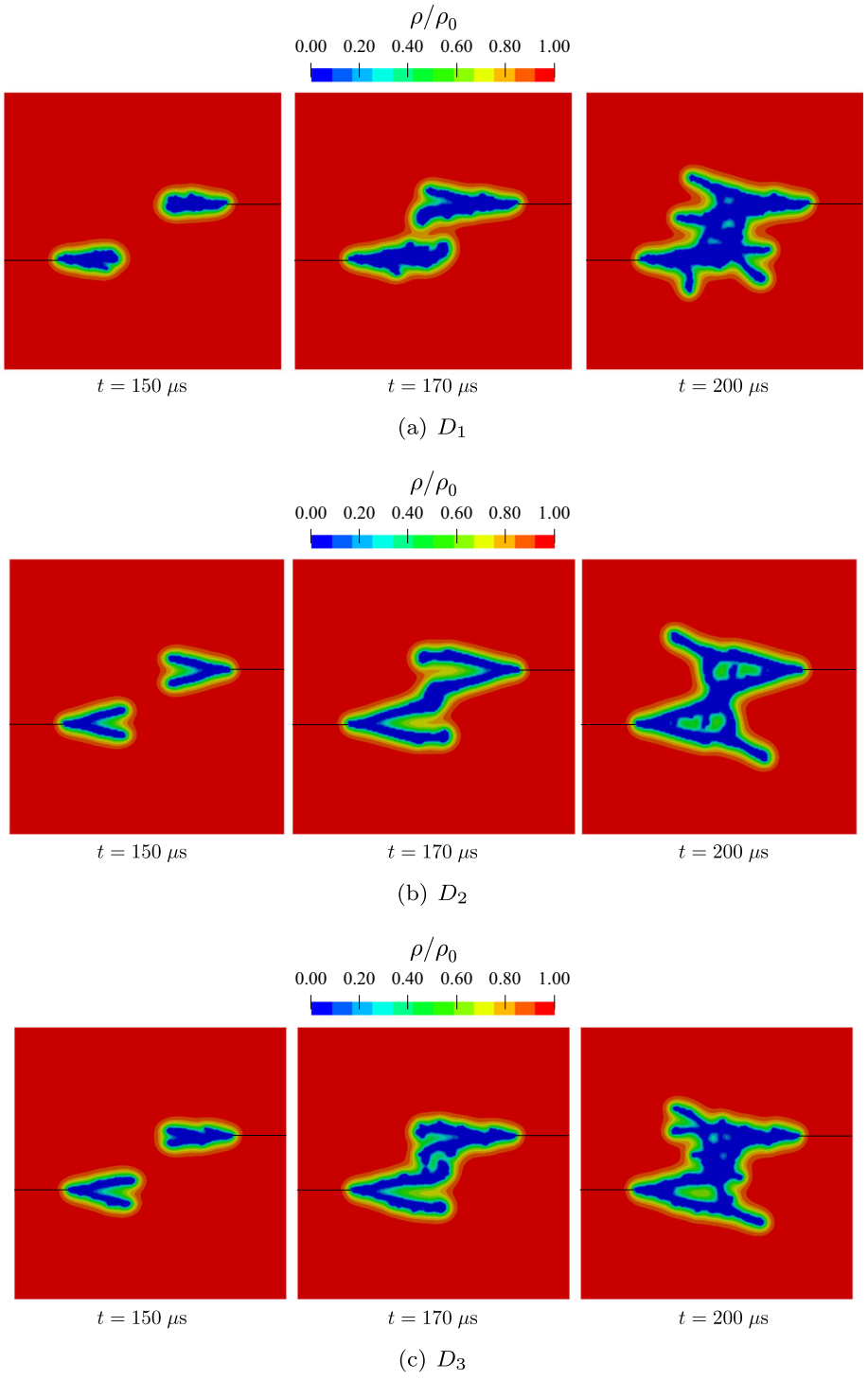

Fig. 12 Double crack problem—case I: contours of ρ/ρ_0 for D_1 to D_3 at $t = 150,\ 170$, and 200 μs. The initial cracks are shown by thick black lines

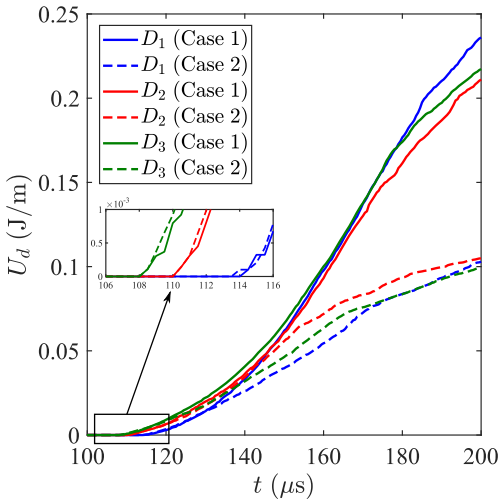

Fig. 13 Dissipation energy for double crack problem

4.1.2 Case II

Unlike case I, for case II inertia of the elements surrounding the crack continuously decreases with the decrease in density. Hence, the crack-tip is always surrounded by a zone of reduced inertia. $\epsilon = 0.05$ is used for element deletion. [1] Contours of ρ/ρ_0 are shown in Fig. 8 for S_1 to S_3 at $t = 167$ μs, in the reference configuration. Corresponding meshes with deleted elements (shown in blue colors) are also shown in the same figure. The fracture patterns are completely different from those observed in case I. S_1 shows multiple (more than two) crack branches, all growing together. For relatively finer meshes (S_2 and S_3) only a main crack, with one or two sub-cracks, is observed. Crack velocity and dissipation energy for S_2 and S_3 are compared in Fig. 9 and they are not very different for both the meshes (S_1 is not compared due to a different crack pattern). Small differences in dissipation energy are due to the different numbers of sub-cracks in S_2 and S_3. Very localized element deletion is observed for case II and hence thickness of the crack is relatively smaller as compared to case I. This is due to the local inertia gradient present in this case near the crack-tip.

To understand more on the effect of local inertia near the crack-tip, stresses ahead of the crack-tip are observed. Figure 10 compares the contours of the opening stress (σ_{yy}) ahead of the crack-tip for cases I and II. Upper and lower halves of Fig. 10 show the stresses for cases I and II, respectively. The stress is plotted at two different time points, one before and one after the failure. At $t = 106$ μs, when there is no failure, cases I and II should be similar as evident from Fig. 10a, showing similar stresses for the upper and lower halves. With further loading, density at the crack-tip starts decreasing, which in-turn results in a decrease in stress for a few elements at the crack-tip. At $t = 112$ μs, stress becomes zero for few element (which are deleted). Now, the crack-tip for case II (lower half) is surrounded by a region of reduced inertia. σ_{yy} at this instant is shown in Fig. 10b. Stress for case I is higher (almost double) than case II. This suggests that even though the change in inertia is very local, its effect on the stress fields around the crack-tip is significant, which leads to overall different crack propagation in cases I and II.

4.2 Double crack problem

Geometry and loading of the problem with two cracks are shown in Fig. 4b. Interactions between the two cracks are analyzed for cases I and II. Similar to the Mode-I crack problem, a full problem is solved. A constant velocity $V_0 = 4$ m/s is applied at the ends $y = \pm 2.5$ mm. Three different meshes, D_1 to D_3, are analyzed, and are shown in Fig. 11. Details of the meshes are given in Table 3.

[1] It should be mentioned here that a higher value of ρ_{cr} is used in case II, compared to that in case I. This is because the current value of density is used for the calculation of the stable time increment in case II. Using $\epsilon = 0.001$ results in extremely small time steps for elements close to the cracked region, unnecessarily slowing down the simulations. For a few cases, simulations have been performed for similar values of ϵ in cases I and II, to ensure that the differences in results between both cases are not only due to different values of ρ_{cr}. For S_2 results for different values of ϵ are shown in Fig. 17 in Appendix 2.

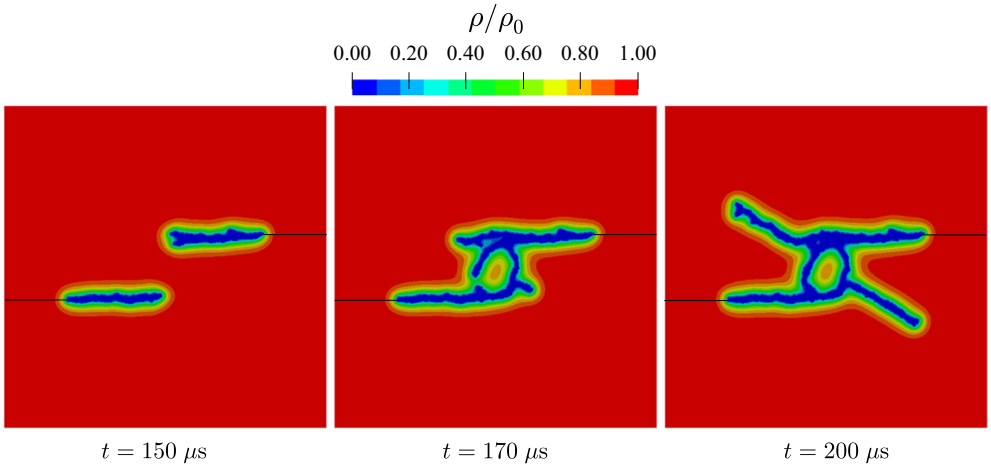

(a) D_1

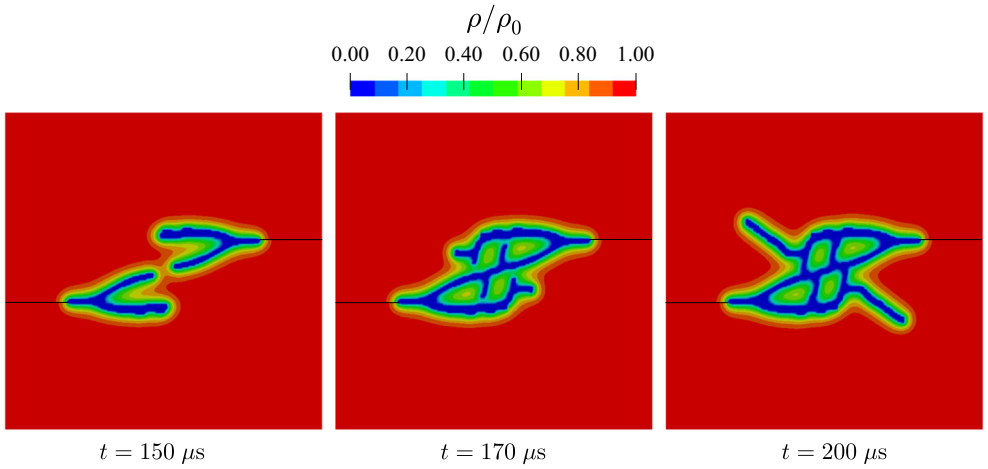

(b) D_2

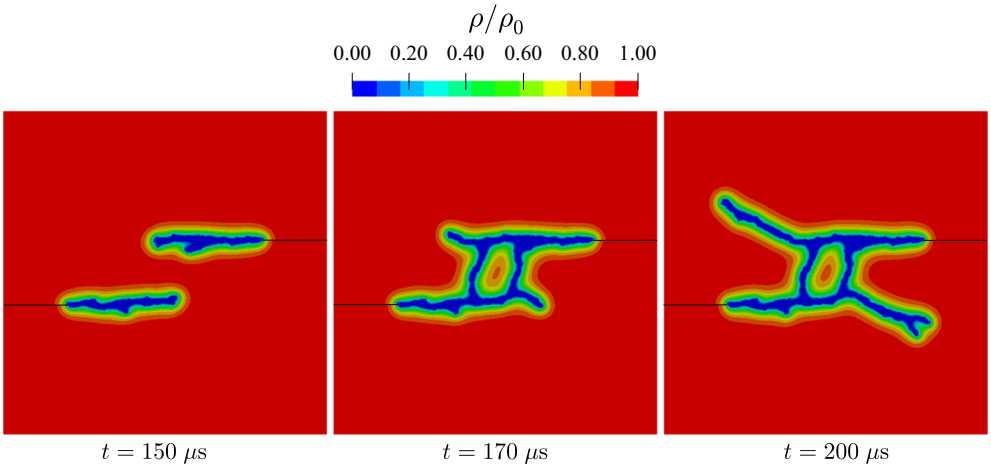

(c) D_3

Fig. 14 Double crack problem—case II: contours of ρ/ρ_0 for D_1 to D_3 at $t = 150,\ 170$, and $200\ \mu$s. Initial cracks are shown by thick black lines

4.3 Case I

Contours of ρ/ρ_0 for this case are shown in Fig. 12 for $D_1 - D_3$, in the reference configuration. For each mesh, status of the cracks is shown at three different time points $t = 150,\ 170$ and $200\ \mu$s. $\epsilon = 0.001\rho_0$ is used. Both the cracks start with branching near their origin. The branches which are close to each other merge together and cause complete separation of the specimen. Due to dynamic effects, cracks keep growing further in each of the fragments.

Regarding the effect of mesh size, most of the observations, which are noted for the Mode-I crack problem (Section 4.1) hold true for this problem also. Symmetry of the solution depends upon the degree of symmetry in the mesh. More sub-cracks and branching are observed as elements become smaller. With mesh becoming finer, the crack patterns seems to converge. However, once the two cracks merge and separation occurs, the formation of sub-cracks in each half is complicated and different for each mesh. Dissipation energy for this case is plotted in Fig. 13 with solid lines. Before the two cracks merge ($\approx t = 170\ \mu$s), dissipation energy for all meshes are close enough. After the separation, different crack patterns in D_1 to D_3 result in deviation from each other, however, energy for D_2 and D_3 are still similar. Crack initiation time decreases with the element becoming smaller, which can be observed in the inset of Fig. 13.

4.4 Case II

Contours of ρ/ρ_0 for this case are shown in Fig. 14 for $D_1 - D_3$, in the reference configuration. $\epsilon = 0.05\rho_0$ is used. The fracture pattern depends upon the mesh. Similar to the Mode-I crack problem, element deletion for case II is very localized. This is also evident from dissipation energy, which is plotted as dashed lines in Fig. 13. Dissipation energies for case II are less than that in case I.

5 Conclusion

Numerical formulation and implementation of the theory suggesting fracture as material sink has been presented. Numerical simulations have been used to reveal the effect of inertia near the crack-tip on the crack growth in dynamic failure processes including problems with single and double cracks. Conclusions of the present study can be grouped as follows:

5.1 Role or inertia

The crack growth pattern completely changes, with and without consideration of decreasing inertia near the crack-tip (case II and case I, respectively). The inertia gradient around the crack-tip results in a weaker stress field at the crack tip and much localized element deletion for case II as compared to case I. Effects of local inertia observed in the present work will also be applicable for phase-field methods used for dynamic fracture. We are pleased to note that the phase field modelers started tending to the same conclusion of the necessity to cancel material inertia together with the material stiffness – see [1] and [8].

5.2 Mesh dependence

First, we should distinguish between *strong* and *weak* mesh dependence.

By the *strong*, we mean the classical pathological mesh dependence, which leads to the decreasing fracture energy with the decreasing mesh size and can culminate in zero energy fracture. Such strong mesh-dependence is suppressed by the present formulation in which failure diffusion is automatically incorporated and the mesh size is always smaller than the characteristic length of diffusion. Energy dissipation during fracture converges with the mesh size refinement.

By the *weak*, we mean the effect of the mesh shape and size on the specific crack pattern. In our simulations, the weak mesh-dependence has been observed even for sufficiently fine meshes. Mesh alterations could trigger various crack patterns for the same amount of the dissipated fracture energy. This observation could probably be explained qualitatively as follows. Fracture in real materials is affected by structural inhomogeneities. The crack path can be different in each specimen made of the same material depending upon distribution of these inhomogeneities. In numerical simulations, the materials are idealized as homogeneous. However, we believe that differences in various mesh structures work as numerical inhomogeneities, which affect the crack path and this is the reason why we observed different crack paths even for different fine meshes.

We should also note that the difference between the strong and weak mesh dependencies has never been pointed to in the literature. Some researchers expect the universal effect of the regularization as a panacea of any mesh sensitivity. While this is definitely true concerning the suppression of the zero energy fracture, generally, there are no reasons to expect a complete and universal fracture pattern emerging from the regularized formulation.

5.3 Material sink versus phase field

Material sink and phase filed approaches have very similar mathematical structure in which the additional variable describing damage obeys additional partial differential equation of the reaction-diffusion type. The spatial gradient term in this equation induces the length scale, which provides the regularization of the fracture modeling. Thus, from the mathematical standpoint, both approaches belong to the same family and a similarity of the outcome of their numerical analyses would not be surprising. At the same time, it should not escape attention of the reader that the material sink formulation is much simpler than numerous and various phase field formulations.

While mathematics of both approaches is similar, the physics is not. The phase field variable and its reaction-diffusion equation do not have any direct physical interpretation. It is just a formal tool to regularize calculations avoiding the zero energy fracture. The situation is different in the mass sink approach in which the mass density is the damage variable and the regularizing reaction-diffusion equation is the classical mass balance law. The clear physical meaning of all variables in the mass sink approach is not a matter of wording; it has a strong implication—the necessity to cancel the inertia forces in the material areas with the decreased stiffness. Physics helps! This difference between the mass sink and phase field approaches is critical for the consideration of dynamic fracture.

Acknowledgments The authors thank Prof. Mahmood Jabareen for introducing them to the CPE formulation and the valuable discussion on it.

Funding information The authors acknowledge the support from the Israel Science Foundation, grant No. ISF-198/15.

Compliance with Ethical Standards

Conflict of interest The authors declare that they have no conflict of interest.

Appendix 1. Results for coarse mesh

Table 4 Details of the meshes S_4 and S_5

	No. of element	Min. edge length (mm)	Avg. min. edge length (mm)
S_4	40000	0.02	0.0213
S_5	32904	0.0117	0.0244

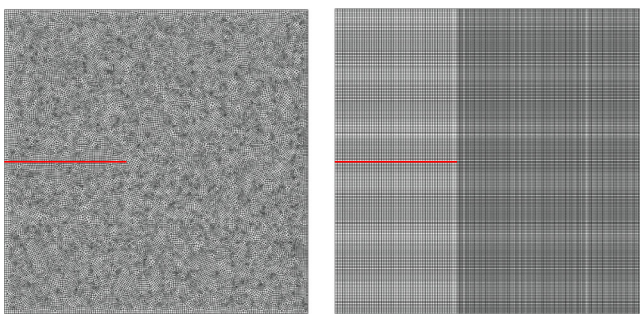

(a) S_4 (b) S_5

Fig. 15 Coarse meshes for single crack problem. Thick red lines indicate the initial cracks

Appendix 2. Effect of critical density on crack propagation

Using similar values of ϵ in cases I and II, crack propagation for mesh S_2 is compared in Fig. 17. For case I, higher value of ϵ results in a slightly thicker crack, whereas, for case II, it changes the crack growth pattern.

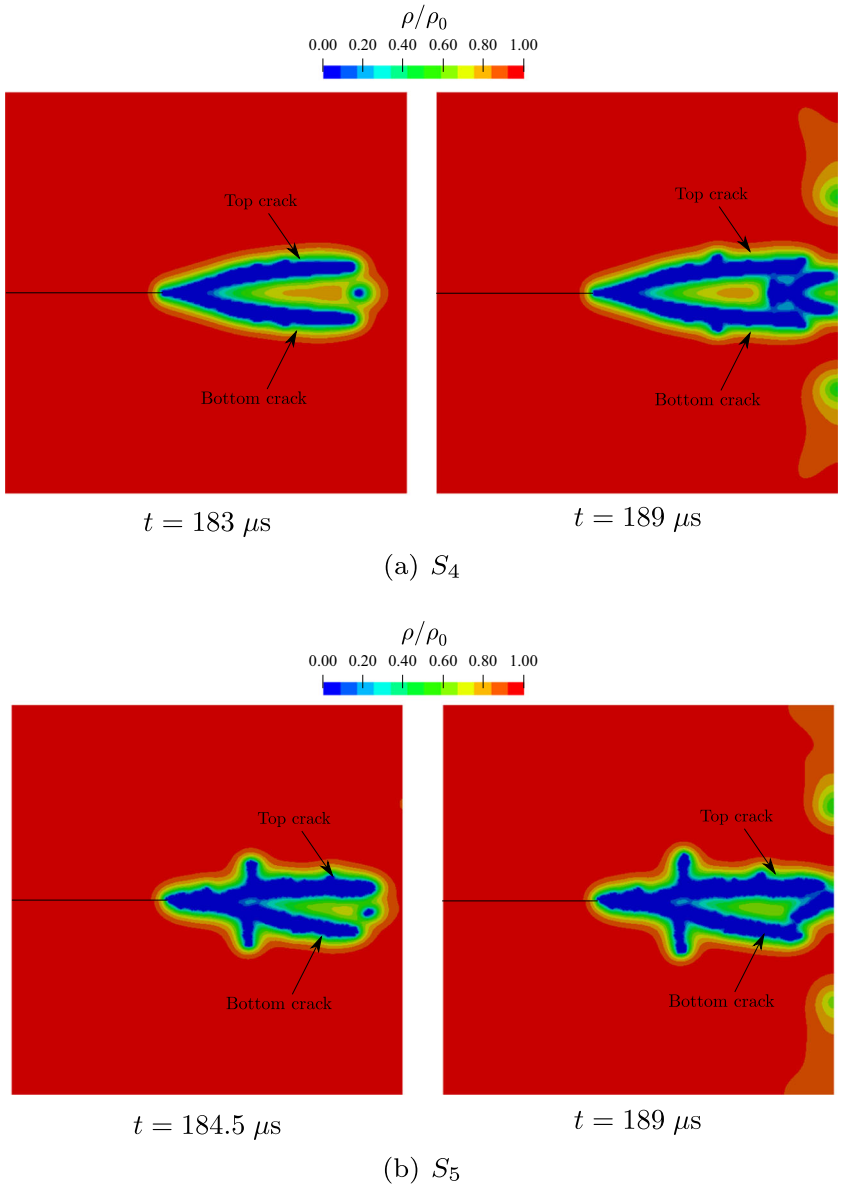

Fig. 16 Mode-I crack problem—case I: contours of ρ/ρ_0 for S_4 and S_5 showing crack growth after the interaction of top and bottom cracks. Initial crack is shown by a thick black line

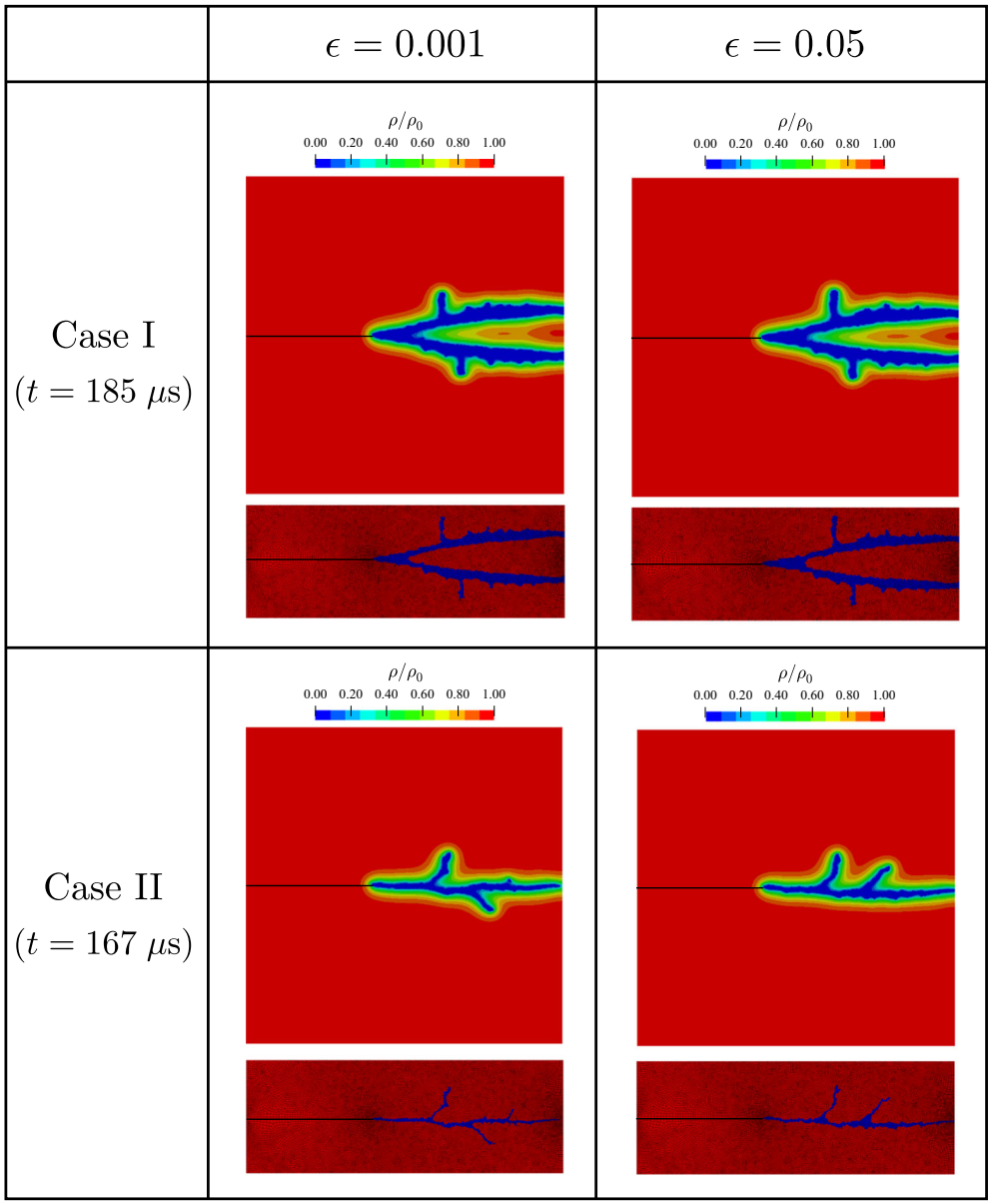

Fig. 17 Effect of critical density on crack growth pattern in mesh S_2 for cases I and II. Initial crack is shown by a thick black line

References

1. Agrawal, V., Dayal, K.: Dependence of equilibrium griffith surface energy on crack speed in phase-field models for fracture coupled to elastodynamics. Int. J. Fract. **207**(2), 243–249 (2017)
2. Barenblatt, G.I.: The formation of equilibrium cracks during brittle fracture. General ideas and hypotheses. Axially-symmetric cracks. J. Appl. Math. Mech. **23**(3), 622–636 (1959)
3. Belytschko, T., Bindeman, L.: Assumed strain stabilization of the 4-node quadrilateral with 1-point quadrature for nonlinear problems. Comput. Methods Appl. Mech. Eng. **88**(3), 311–340 (1991)
4. Belytschko, T., Bindeman, L.P.: Assumed strain stabilization of the eight node hexahedral element. Comput. Methods Appl. Mech. Eng. **105**(2), 225–260 (1993)
5. Benzerga, A.A., Leblond, J.B., Needleman, A., Tvergaard, V.: Ductile failure modeling. Int. J. Fract. **201**(1), 29–80 (2016)
6. Borden, M.J., Verhoosel, C.V., Scott, M.A., Hughes, T.J.R., Landis, C.M.: A phase-field description of dynamic brittle fracture. Comput. Methods Appl. Mech. Eng. **217**, 77–95 (2012)

7. Camacho, G.T., Ortiz, M.: Computational modelling of impact damage in brittle materials. Int. J. Solids Struct. **33**(20-22), 2899–2938 (1996)
8. Chen, C.H., Bouchbinder, E., Karma, A.: Instability in dynamic fracture and the failure of the classical theory of cracks. Nat. Phys. **13**(12), 1186 (2017)
9. De Borst, R.: Some recent issues in computational failure mechanics. Int. J. Numer. Methods Eng. **52**(1-2), 63–95 (2001)
10. De Borst, R., Van Der Giessen, E.: Material Instabilities in Solids. Wiley, Chichester (1998)
11. Dolbow, J., Belytschko, T.: A finite element method for crack growth without remeshing. Int. J. Numer. Methods Eng. **46**(1), 131–150 (1999)
12. Dorfmann, A., Ogden, R.W.: A constitutive model for the mullins effect with permanent set in particle-reinforced rubber. Int. J. Solids Struct. **41**(7), 1855–1878 (2004)
13. Francfort, G.A., Marigo, J.J.: Revisiting brittle fracture as an energy minimization problem. J. Mech. Phys. Solids **46**(8), 1319–1342 (1998)
14. Gong, B., Paggi, M., Carpinteri, A.: A cohesive crack model coupled with damage for interface fatigue problems. Int. J. Fract. **173**(2), 91–104 (2012)
15. Gurson, A.L.: Continuum theory of ductile rupture by void nucleation and growth: Part I. Yield criteria and flow rules for porous ductile media. J. Eng. Mater. Technol. **99**(1), 2–15 (1977)
16. Hofacker, M., Miehe, C.: Continuum phase field modeling of dynamic fracture: variational principles and staggered FE implementation. Int. J. Fract. **178**(1-2), 113–129 (2012)
17. Jabareen, M., Rubin, M.: Hyperelasticity and physical shear buckling of a block predicted by the cosserat point element compared with inelasticity and hourglassing predicted by other element formulations. Comput. Mech. **40**(3), 447–459 (2007)
18. Kachanov, L.M.: Time of the rupture process under creep conditions, izy akad. Nank SSR Otd Tech Nauk **8**, 26–31 (1958)
19. Karma, A., Kessler, D.A., Levine, H.: Phase-field model of mode iii dynamic fracture. Phys. Rev. Lett. **87**(4), 045,501 (2001)
20. Klein, P., Gao, H.: Crack nucleation and growth as strain localization in a virtual-bond continuum. Eng. Fract. Mech. **61**(1), 21–48 (1998)
21. Lasry, D., Belytschko, T.: Localization limiters in transient problems. Int. J. Solids Struct. **24**(6), 581–597 (1988)
22. Lemaitre, J., Desmorat, R.: Engineering Damage Mechanics: Ductile, Creep, Fatigue and Brittle Failures. Springer, Berlin (2005)
23. Menzel, A., Steinmann, P.: A theoretical and computational framework for anisotropic continuum damage mechanics at large strains. Int. J. Solids Struct. **38**(52), 9505–9523 (2001)
24. Mtanes, E., Jabareen, M.: A plane strain quadrilateral cosserat point element (cpe) for nonlinear orthotropic elastic materials: An extension to initially distorted geometry and general orthotropic directions. Finite Elem. Anal. Des. **87**, 10–21 (2014)
25. Needleman, A.: A continuum model for void nucleation by inclusion debonding. J. Appl. Mech. **54**(3), 525–531 (1987)
26. Needleman, A.: Some issues in cohesive surface modeling. Procedia IUTAM **10**, 221–246 (2014)
27. Park, K., Paulino, G.H., Roesler, J.R.: A unified potential-based cohesive model of mixed-mode fracture. J. Mech. Phys. Solids **57**(6), 891–908 (2009)
28. Peerlings, R.H.J., De Borst, R., Brekelmans, W.A.M., De Vree, J.H.P.: Gradient enhanced damage for quasi-brittle materials. Int. J. Numer. Methods Eng. **39**, 3391–3403 (1996)
29. Peerlings, R.H.J., De Borst, R., Brekelmans, W.A.M., De Vree, J.H.P., Spee, I.: Some observations on localisation in non-local and gradient damage models. Eur. J. Mech. A. Solids **15**(6), 937–953 (1996)
30. Peerlings, R.H.J., Brekelmans, W.A.M., De Borst, R., Geers, M.G.D.: Softening, singularity and mesh sensitivity in quasi-brittle and fatigue damage, in nonlocal aspects in solid mechanics. In: Proceedings of EUROMECH Colloquium, vol. 378, pp. 94-99 (1998)
31. Peerlings, R.H.J., De Borst, R., Brekelmans, W.A.M., Geers, M.G.D.: Localisation issues in local and nonlocal continuum approaches to fracture. Eur. J. Mech. A. Solids **21**(2), 175–189 (2002)
32. Pian, T.H., Sumihara, K.: Rational approach for assumed stress finite elements. Int. J. Numer. Methods Eng. **20**(9), 1685–1695 (1984)
33. Pijaudier-Cabot, G., Bažant, Z.P.: Nonlocal damage theory. J. Eng. Mech. **113**(10), 1512–1533 (1987)
34. Raghavan, M.L., Vorp, D.A.: Toward a biomechanical tool to evaluate rupture potential of abdominal aortic aneurysm: identification of a finite strain constitutive model and evaluation of its applicability. J. Biomech. **33**(4), 475–482 (2000)
35. Rice, J.R., Wang, J.S.: Embrittlement of interfaces by solute segregation. Mater. Sci. Eng. A **107**, 23–40 (1989)
36. Silling, S.A.: Reformulation of elasticity theory for discontinuities and long-range forces. J. Mech. Phys. Solids **48**(1), 175–209 (2000)
37. Simo, J., Armero, F., Taylor, R.: Improved versions of assumed enhanced strain tri-linear elements for 3d finite deformation problems. Comput. Methods Appl. Mech. Eng. **110**(3-4), 359–386 (1993)
38. Simo, J.C.: On a fully three-dimensional finite-strain viscoelastic damage model: formulation and computational aspects. Comput. Methods Appl. Mech. Eng. **60**(2), 153–173 (1987)
39. Simo, J.C., Armero, F.: Geometrically non-linear enhanced strain mixed methods and the method of incompatible modes. Int. J. Numer. Methods Eng. **33**(7), 1413–1449 (1992)
40. Taylor, R.L.: FEAP - finite element analysis program. http://www.ce.berkeley/feap (2014)
41. Taylor, R.L.: FEAP - finite element analysis program: Version 8.4 programmer manual. http://www.ce.berkeley/feap/pmanual84.pdf (2014)
42. Taylor, R.L.: FEAP - finite element analysis program: Version 8.4 user manual. http://www.ce.berkeley/feap/manual84.pdf (2014)
43. Tvergaard, V., Hutchinson, J.W.: The relation between crack growth resistance and fracture process parameters in elastic-plastic solids. J. Mech. Phys. Solids **40**(6), 1377–1397 (1992)
44. Volokh, K.Y.: Nonlinear elasticity for modeling fracture of isotropic brittle solids. J. Appl. Mech. **71**(1), 141–143 (2004)
45. Volokh, K.Y.: Hyperelasticity with softening for modeling materials failure. J. Mech. Phys. Solids **55**(10), 2237–2264 (2007)
46. Volokh, K.Y.: Review of the energy limiters approach to modeling failure of rubber. Rubber Chem. Technol. **86**(3), 470–487 (2013)
47. Volokh, K.Y.: Mechanics of Soft Materials. Springer, Singapore (2016)
48. Volokh, K.Y.: Fracture as a material sink. Materials Theory **1**(1), 3 (2017)
49. Voyiadjis, G.Z., Kattan, P.I.: A plasticity-damage theory for large deformation of solids-I. theoretical formulation. Int. J. Eng. Sci. **30**(9), 1089–1108 (1992)
50. Xu, X.P., Needleman, A.: Numerical simulations of fast crack growth in brittle solids. J. Mech. Phys. Solids **42**(9), 1397–1434 (1994)